Share Your Innovations through JACS Directory

Journal of Nanoscience and Technology

Visit Journal at http://www.jacsdirectory.com/jnst

ISSN: 2455-0191

Structural and Dielectric Investigations of Cerium Stabilized Zirconia ($Zr_{1-x}Ce_xO_2$(x=0-0.05)) Nanocrystals Blended by Wet Chemical Method

H.C. Madhusudhana[1,2,*], S.N. Shobhadevi[3], B.M. Nagabhushana[4], R. Hari Krishna[4], M.V. Murugendrappa[5], H. Nagabhushana[6]

[1]*Department of Physics, Dayananda Sagar Academy of Technology and Management, Bangalore – 560 082, Karnataka, India.*
[2]*B.M.S. Academy of Science and Research affiliated to Tumkur University, Bangalore – 560 019, Karnataka, India.*
[3]*Department of Physics, B.M.S. College for Women, Bangalore – 560 019, Karnataka, India.*
[4]*Department of Chemistry, M.S. Ramaiah Institute of Technology, Bangalore – 560 054, Karnataka, India.*
[5]*Department of Physics, B.M.S College of Engineering, Bangalore – 560 019, Karnataka, India.*
[6]*C.N.R.Center for Nano Research, Tumkur University, Tumkur – 572 103, Karnataka, India.*

ARTICLE DETAILS

Article history:
Received 20 March 2019
Accepted 15 April 2019
Available online 05 May 2019

Keywords:
Solution Combustion
Ce^{3+} Doped ZrO_2
AC Conductivity

ABSTRACT

Cerium doped ZrO_2 nano crystals ($Zr_{1-x}Ce_xO_2$(x=0-0.05)) have been synthesized by solution combustion method using glycine as a fuel at furnace temperature 400 °C. The obtained samples are characterized by X-ray diffraction, scanning electron microscopy, and Fourier transform infrared spectroscopy, UV-Vis-spectroscopy and AC conductivity techniques. The XRD patterns exhibit decrease in crystallinity of the sample with increase in dopant concentration. The crystallite size is found to be 20-30 nm. The particle size is decreasing with Ce^{3+} concentration. The SEM analysis reveals change of porosity and shape of ZrO_2 samples from spherical grain structure at 1 mol% of Ce^{3+} to irregular flake like structures in shape at 5 mol% of Ce^{3+}. The band gap is decreasing from 4 to 3.3 eV as the doping concentration increases. AC impedance spectroscopy results of the as synthesized Ce doped ZrO_2 shows good dielectric properties with a very high dielectric constant. Sample of ZrO_2 doped with 5 mol% Ce^{3+} is found to have high dielectric constant (ε' = 50) and the lowest dielectric constant (ε' = 18) is found for undoped ZrO_2 at 10 MHz. The lowest dielectric loss is measured for the sample having 5 mol% cerium doped zirconia.

1. Introduction

Zirconia has likely the richest folks of nanostructures between all materials. Recently, nanocrystalline ceramics and the application of nanoparticles to develop the ceramic properties have created great interest, as the mechanical, electrical and magnetic properties are crystallite size responsive. Nanoparticles have expected much consideration in the field of material science because of their smart mechanical and physico-element properties which are completely different from their bulk counterparts [1-4]

Cerium incorporated ZrO_2 that generally is used for several resolves related reduction process, such as oxygen reservoir and ionic conductor [5]. The chemical properties of cerium which has two oxidation states 3^+ and 4^+, makes it possible that large amount of reduction process. When oxygen partial pressure is high, cerium is fully oxidized and become 4^+ states. On the other hands, when oxygen partial pressure is low, cerium is deoxidized and become 3^+ states. Therefore, cerium-doped ZrO_2 can store oxygen by change of partial pressure of oxygen or conduction of oxygen ion. Since application area of cerium-doped ZrO_2 is closely related with its chemical state, chemical property of cerium-doped ZrO_2 is intensively researched in many articles [6].

2. Experimental Methods

2.1 Chemicals

Analytical grade zirconyl nitrate [ZrO $(NO_3)_2.6H_2O$: 99.99%] (Central Drug House (p) Ltd.), cerium nitrate [$Ce(NO_3)_3.6H_2O$: 98.99%] (Central Drug House (p) Ltd.) and glycine [$C_2H_5NO_2$: 99.98%] (Sigma Aldrich (p) Ltd.) are used as a starting materials for the preparation of Ce doped ZrO_2 nanoparticles. The chemicals are used without any further purification.

2.2 Synthesis

For the synthesis of cerium doped zirconia, the stoichiometric amount of the samples used for combustion is calculated using total oxidizing and reducing valences of compounds. Calculated amount of zirconyl nitrate and glycine was added along with 25 mL of deionized water and the mixture was continuously stirred at room temperature up to get the homogeneous mixture. Later cerium nitrate was added to the mixture and mixed thoroughly to obtain the aqueous solution. The redox mixture was taken in a crystalline dish and introduced in a preheated muffle furnace maintained at 400 °C. Initially the solution boils and undergoes dehydration. Eventually the mixture undergoes decomposition, which results in the liberation of large amounts of gases (CO_2, N_2). This was followed by a spontaneous ignition which resulted in flame type combustion with enormous swelling of the reaction mixture, which in turn produces foamy and voluminous ZrO_2:Ce^{3+} (1-5 mol%).

2.3 Characterization

The powder X-ray diffraction (PXRD) patterns were recorded on X-ray diffractometer (Bruker AXS D8 Advance) using Cu k_α radiation (λ=1.5418 Å) in the 2θ range 20° - 80°. Raman spectroscopy done by Horiba Jobin Yvon labRam HR in the range 0 to 800 cm^{-1}. The FTIR spectra of the ZrO_2 were recorded on IR Affinity-1 (Shimadzu, Japan) spectrometer in KBr medium, at room temperature. Energy gap analysis by UV-visible spectrometer (Specord 250 plus, Germany). SEM micrographs were studied using scanning electron microscope (Jeol 6390 LV). HRTEM analysis was carried out by High resolution transmission electron microscope (300 kV, FEI, Technai G2, F30 S-Twin with FEG source). Nitrogen adsorption and desorption studies were carried out by BET surface area analyzer (NOVA.1000 Ver.370, USA). For impedance measurements, 1.0 g of each sample was pelletized to a diameter of about 10.0 mm and thickness of 1.0 mm. The pressure applied was about 10

*Corresponding Author:msudhan01@gmail.com(H.C. Madhusudhana)

https://doi.org/10.30799/jnst.220.19050201

tons/sqm. The pellets were then sintered in vacuum at 300 °C for 3 hours. The pelletized samples were analyzed by spectroscopy using 6500B series of precision impedance analyzer (Wayne Kerr-UK Electronics Pvt. Ltd., India) in the frequency range from 20 Hz to 10^7 Hz at room temperature. DC conductivity is measured using two probe technique (SES Instruments Pvt. Ltd). The frame contains the supporting electrodes made of Boller steel which enables to take observations even at temperatures as high as 700 °C. The pellet of sample under study can be sand-witched between two brass electrodes.

3. Results and Discussion

The XRD patterns of $Zr_{1-x}Ce_xO_2$ (x=0-0.05) are as shown in the Fig. 1 and the diffraction peaks of the samples are indexed as (1 1 1), (2 0 0), (2 2 0), (3 1 1), (2 2 2) and (4 0 0) respectively for 30.19°, 34.93°, 50.29°, 59.88°, 62.42° and 73.51°. The diffraction peaks of the sample are well resolved, highly intense and sharp matching with the standard JCPDS file No.27-0997 confirming the crystal structure as the cubic phase which is also in conformity with previous reports by S. Manjunatha et.al [5]. At x=0.0, zirconia showed more intense peaks with wide base but as the doping concentration increased intensity of the peaks decreased and the base became more widened after x=0.2.

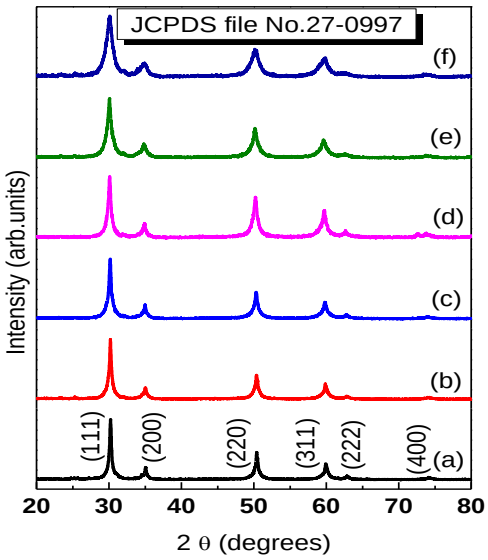

Fig. 1 XRD patterns of $Zr_{1-x}Ce_xO_2$ at (a) undoped (b) x=0.01 (c) x=0.02 (d) x=0.03 (e) x=0.04 and (f) x= 0.05

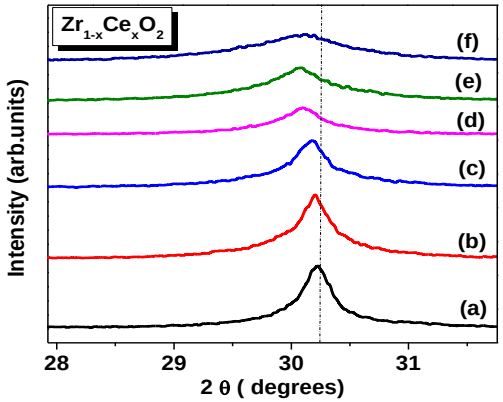

Fig. 2 Shifting of XRD peaks of $Zr_{1-x}Ce_xO_2$ at (a) undoped (b) x=0.01 (c) x=0.02 (d) x=0.03 (e) x=0.04 and (f) x= 0.05 molar concentrations

Fig. 2 shows the peak shifting towards the lower angle side as the doping concentration increased which indicates that Ce^{3+}ions (radius 1.07 Å) are replacing Zr^{4+} ions (0.74 Å) which in turn decrease the crystallite size. Scherrer's equation was used to calculate the crystallite size of the samples [7].

$$D = \frac{K\lambda}{\beta Cos\theta} \quad (1)$$

where D represents crystallite size, K is constant (~ 0.94), β is full width half maximum and θ stands for Bragg's angle. Using Bragg's law ($n\lambda = 2dsin\theta$) interplanar spacing was calculated and is compared with the standard JCPDS data for the order n=1. The lattice constant (a) and dislocation density (δ) were also calculated using the Eqs.(2) and (3). The complete details of the calculated data are listed in the Table 1.

$$d_{hkl} = \frac{a}{\sqrt{h^2+k^2+l^2}} \quad (2)$$

$$\delta = \frac{1}{D^2} \quad (3)$$

Table 1 Crystallite size, Bandgap and strain of both methods (Scherrer's & W-H method)

ZrO_2:Ce^{3+} (mol%)	Crystallite size (nm)			
	Scherrer's method	W-H method	Band gap (eV)	Strain (ε) x 10^{-3}
0	23	25	4.0	16.90
1	21	22	3.8	18.02
2	19	19	3.6	20.21
3	17	18	3.5	22.89
4	12	15	3.4	31.79
5	8	10	3.3	50.54

It was observed that the d-spacing increased from 2.954 Å to 2.965 Å and the dislocation density also increased from 1.50 x $10^{15}/m^2$ to 12 x $10^{15}/m^2$. To verify this, a method suggested by Williamson and Hall (W-H) was followed [8] and this method is applicable in the cases where both crystallite size effect and the lattice deformation are simultaneously operative. The combined effect of size and lattice deformation gives rise to the observed full width half maximum (FWHM, β) in the XRD patterns. β is the sum of β_1 (grain size dependent broadening) and β_2 (lattice distortion dependent broadening). W-H equation may be expressed in the form:

$$\beta \cos\theta = \varepsilon\,(4 \sin\theta) + \frac{\lambda}{D} \quad (4)$$

where β (in radian), ε is the strain developed and D is the grain size. The equation represents a straight line between 4sinθ (x-axis) and βcosθ (y-axis), where 2θ is the Bragg's angle corresponding to XRD peaks. The slope of line gives the strain (ε) and intercept (λ/D) of this line on the Y-axis gives grain size (D). W-H plot for the samples are as shown in the Fig. 3. The detailed calculation of crystallite size and strain of both methods (Scherrer's & W-H method) are listed in the Table 2.

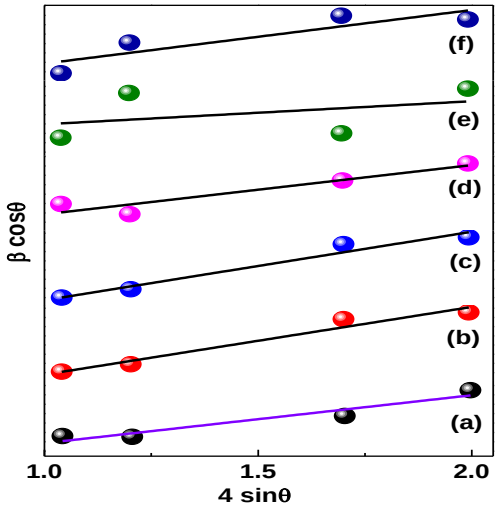

Fig. 3 W-H plots of $Zr_{1-x}Ce_xO_2$ at (a) undoped (b) x=0.01 (c) x=0.02 (d) x=0.03 (e) x=0.04 and (f) x= 0.05 molar concentrations

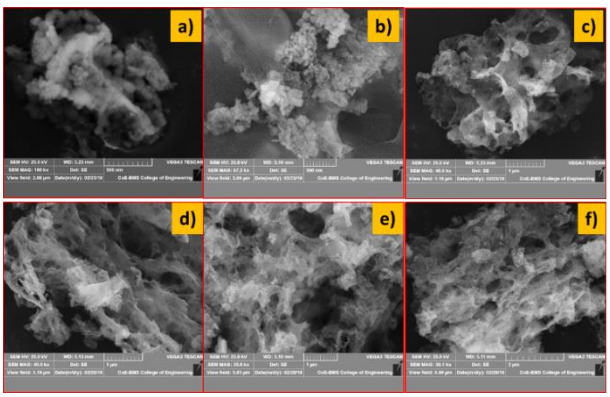

Fig. 4 SEM images of $Zr_{1-x}Ce_xO_2$ at (a) undoped (b) x=0.01 (c) x=0.02 (d) x=0.03 (e) x=0.04 and (f) x= 0.05 molar concentrations

https://doi.org/10.30799/jnst.220.19050201

Cite this Article as: H.C. Madhusudhana, S.N. Shobhadevi, B.M. Nagabhushana, R. Hari Krishna, M.V. Murugendrappa, H. Nagabhushana, Structural and dielectric investigations of cerium stabilized zirconia ($Zr_{1-x}Ce_xO_2$(x=0-0.05)) nanocrystals blended by wet chemical method, J. Nanosci. Tech. 5(2) (2019) 649–654.

SEM provides complementary evidence of different nanostructures. Fig. 4a shows spherical shaped particles which are completely agglomerated in nature. As the doping concentration of Ce increased the shape of the spherical particles changed to irregular non uniform spike like structures (Fig. 4c-f) with high porosity.

Table 2 The detailed calculation of crystallite size and strain of both methods (Scherrer's and W-H method)

Sample	(hkl)	2θ° ± 0.01	d_{XRD} (Å)	d_{JCPDS} (Å)	Error in d	FWHM	a (Å)	D(nm) ± 1	δ (10^{15}/m²)
Undoped	111	30.22	2.954	2.930	0.024	0.319	5.116	25.78	1.504
ZrO_2	200	35.09	2.554	2.550	0.004	0.321	5.108	25.94	1.486
	220	50.39	1.808	1.801	0.007	0.394	5.116	22.27	2.016
	311	59.90	1.542	1.534	0.008	0.483	5.115	18.97	2.778
	222	62.93	1.475	1.471	0.004	-	5.110	-	
	400	74.20	1.276	1.270	0.006	-	5.106	-	
ZrO_2:Ce^{3+}	111	30.31	2.945	2.930	0.015	0.360	5.101	22.84	1.916
(1 mol	200	34.98	2.562	2.550	0.012	0.370	5.124	22.50	1.975
%)	220	50.22	1.814	1.801	0.013	0.405	5.132	21.66	2.131
	311	59.96	1.540	1.534	0.006	0.441	5.110	20.78	2.315
	222	62.93	1.475	1.471	0.004	-	5.110	-	
	400	74.12	1.277	1.270	0.007	-	5.110	-	
ZrO_2:Ce^{3+}	111	30.21	2.954	2.930	0.014	0.330	5.117	24.92	1.610
(2 mol	200	34.98	2.562	2.550	0.012	0.365	5.124	22.81	1.921
%)	220	50.32	1.811	1.801	0.011	0.557	5.122	15.75	4.031
	311	59.69	1.547	1.534	0.013	0.612	5.131	15.08	4.397
	222	62.76	1.478	1.471	0.007	-	5.122	-	
	400	74.12	1.277	1.270	0.007	-	5.110	-	
ZrO_2:Ce^{3+}	111	30.12	2.963	2.930	0.033	0.474	5.132	17.35	3.321
(3 mol	200	34.81	2.574	2.550	0.024	0.451	5.148	18.45	2.937
%)	220	50.12	1.817	1.801	0.016	0.584	5.141	15.15	4.356
	311	59.68	1.547	1.534	0.013	0.458	5.132	19.99	2.502
	222	62.56	1.482	1.471	0.011	-	5.137	-	
	400	73.75	1.283	1.270	0.013	-	5.132	-	
ZrO_2:Ce^{3+}	111	30.11	2.964	2.930	0.030	0.622	5.134	13.28	5.670
(4 mol	200	34.81	2.574	2.550	0.020	0.689	5.148	12.10	6.830
%)	220	50.12	1.817	1.801	0.016	0.675	5.141	13.07	5.853
	311	59.68	1.547	1.534	0.013	0.765	5.132	12.00	6.944
	222	62.76	1.478	1.471	0.007	-	5.122	-	
	400	73.75	1.283	1.270	0.013	-	5.132	-	
ZrO_2:Ce^{3+}	111	30.10	2.965	2.930	0.035	0.928	5.136	8.85	12.76
(5 mol	200	34.81	2.574	2.550	0.024	1.186	5.148	7.42	18.16
%)	220	50.12	1.817	1.801	0.016	1.040	5.141	8.02	15.54
	311	59.68	1.547	1.534	0.013	1.221	5.132	7.50	17.77
	222	62.76	1.478	1.471	0.007	-	5.122	-	
	400	73.35	1.289	1.270	0.019	-	5.156	-	

This type of porous network is a typical characteristic feature of combustion synthesized powders. The porous powders are highly friable which facilitates easy grinding to obtain finer particles. When the gas escapes with high pressure, pores are formed with the simultaneous formation of small particles near the pores [9]. EDS results of 5 mol% Ce^{3+} doped zirconia is as shown in the Fig. 5 on the basis of EDS peaks it can be concluded that amount of zirconia on the surface layer decreases, whereas increase of Ce^{3+} amounts is observed. The detailed compositions of all Ce^{3+} doped ZrO_2 are listed in the Table 3.

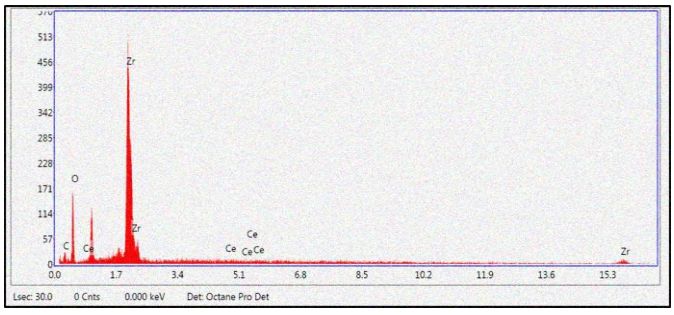

Fig. 5 EDS images of $Zr_{1-x}Ce_xO_2$ at x= 0.05 molar concentration

Table 3 The detailed compositions of all Ce^{3+} doped ZrO_2

Element	X=0.01		X=0.02		X=0.03		X=0.04		X=0.05	
	Weight %	Atomic %	Weight %	Atomic %	Weight %	Atomic %	Weight %	Atomic %	Weight %	Atomic %
C K	13.4	26.18	17.42	34.78	29.66	51.12	16.18	33.62	14.3	30.02
O K	42.76	62.71	35.39	53.05	30.98	40.08	34.18	53.31	36.15	56.98
ZrL	41.95	10.79	44.51	11.7	37.8	8.58	44.23	12.1	42.3	11.69
CeL	1.89	0.32	2.68	0.46	1.56	0.23	5.41	0.96	7.25	1.3
Total	100	100	100	100	100	100	100	100	100	100

The FTIR spectra $Zr_{1-x}Ce_xO_2$ (x=0-0.05) are shown in Fig. 6. The strong broad peaks corresponding to 3445 cm^{-1} and 1624 cm^{-1} confirm the presence hydroxyl group i.e. stretching and bending vibrations of O-H bond due to absorption of water molecules [10]. The intense peak at 1369 cm^{-1} can be attributed to adsorption of non-bridging O-H. The band at 1141 cm^{-1} corresponds to the stretching vibrations of Zr-O^- terminal groups (O^- means a non-bridging atom). A similar observation has been reported by Prakash babu et al [9]. The strong broad peak at 500 cm^{-1} is due to stretching vibrations of Zr-O.

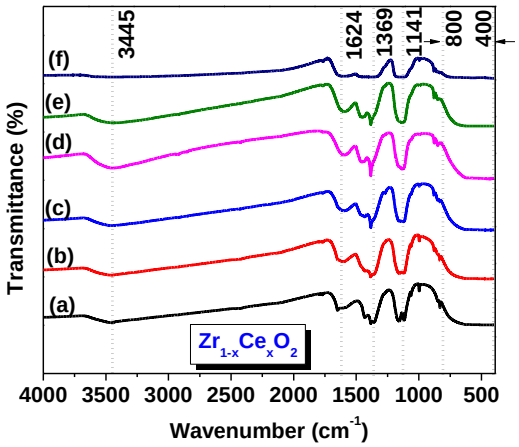

Fig. 6 FTIR spectra of $Zr_{1-x}Ce_xO_2$ at (a) undoped (b) x=0.01 (c) x=0.02 (d) x=0.03 (e) x=0.04 and (f) x= 0.05 molar concentrations

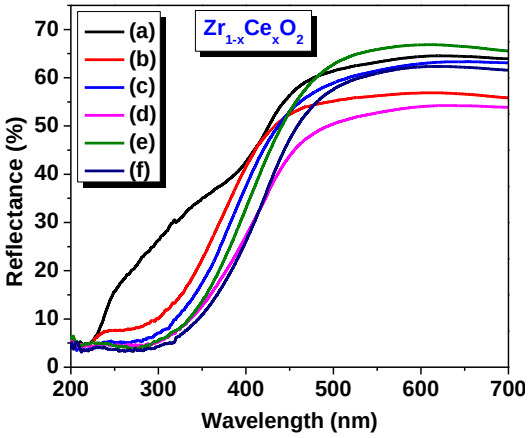

Fig. 7 Reflectance spectra of $Zr_{1-x}Ce_xO_2$ at (a) undoped (b) x=0.01 (c) x=0.02 (d) x=0.03 (e) x=0.04 and (f) x= 0.05 molar concentrations

The UV-Visible analysis was done using reflectance spectra as shown in the Fig. 7. Here it was observed that minimum reflection was between 200-230 nm which is attributed to the transition of charge transfer between O^{2-} (2p) to Zr^{4+} (4d). This transition is mainly due to the excitation of electrons from valence band to conduction band.

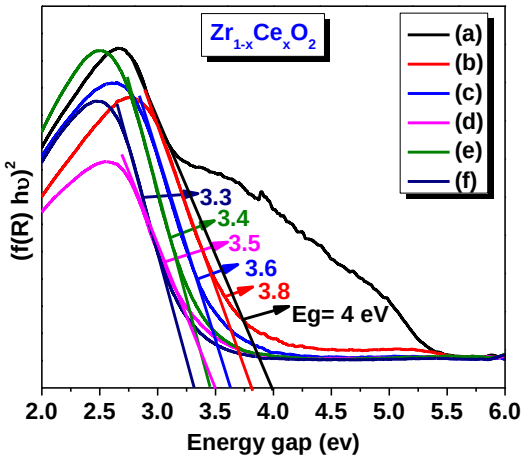

Fig. 8 Kubelka-Munk plot for of $Zr_{1-x}Ce_xO_2$ at (a) undoped (b) x=0.01 (c) x=0.02 (d) x=0.03 (e) x=0.04 and (f) x= 0.05 molar concentrations

In Fig. 8, the Kubelka– Munk function [11,12] was used to calculate the bandgap and it was found that energy decreased due to doping of Ce to ZrO_2 which matches with the previously reported values, 3.3 eV - 4 eV [13, 14]. The drastic decrease in the E_g values is attributed to the introduction

https://doi.org/10.30799/jnst.220.19050201

of more defects in the lattice of ZrO_2 by the interstitials or oxygen vacancies [5].

Impedance spectrometry (IS) is a very suitable and potential experimental tool which enables to correlate the dielectric properties of a material with its microstructure and also it aids to analyse and reprint the contribution from various components (i.e., through grain, grain boundary, interfaces, etc.) of polycrystalline materials over a widespread frequency [15]. The data of resistive (real part) and reactive (imaginary part) components are taken by using Ohmic resistance measurements. It can be presented conventionally in Nyquist plot in terms of any of the four possible complex formalisms, the impedance (Z'), the permittivity (ε'), the admittance (Y') and the dielectric loss (tan δ). The impedance measurements were carried out at room temperature in the frequency range from 100 Hz to 5 MHz.

The Nyquist plots for both undoped and doped samples of zirconia at room temperature are as shown in the Fig. 9 (a-f). The plot exhibits a semicircle from high to medium frequencies indicating the charge transfer process. The straight line, at around 45° of the real axes, observed in the low frequency region, is associated to the semi-infinite Warburg impedance. In addition, the steep sloping line observed in lower frequency region is associated with the finite space diffusion process. The intercept at real impedance (Real- Z) axis on high frequency is related to the ohmic resistance, which comes from the contribution of electrolyte and the electrode [16]. The electrode, grain boundary and grain conductivity contributions were represented by the low, middle order and high frequency semicircles respectively in the Nyquist plots [17]. Hence, the total conductivity is due to electrode, grain boundary and grain contributions. From EC-Lab software (version 11.12) Biologic instruments, the electrochemical parameters were evaluated.We witnessed excellent agreement between the parameters obtained from the fitting results (electrical equivalent circuit model) and experimental results. The chi-squared (χ^2) minimized to 10^{-3}. $\chi^2$is the function defined as the sum of the squares of the residuals. The electrical equivalent circuit was used in simulation of the impedance behaviour of the samples from the experimentally obtained impedance data. The corresponding circuit to fit the impedance graphs is represented in the inset of Fig. 9(a-f).

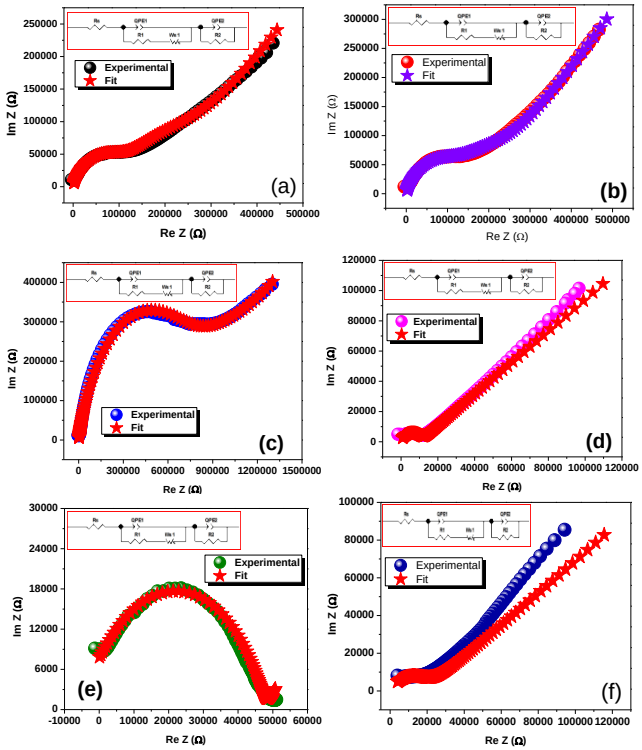

Fig. 9 Nyquist plots for (a) undoped, (b) 1 mol% Ce^{3+}, (c) 2 mol%, (d) 3 mol% Ce^{3+}, (e) 4 mol% and (f) 5 mol% Ce^{3+} doped samples of zirconia at room temperature

The model $R_s+Q_1/(R_1+W_1)+Q_2/R_2$ is fitted for undoped and Ce^{3+}doped ZrO_2 samples. It consists of a series combination of solution resistance R_s and constant phase element Q_1 which is in parallel with resistor R_1 and Warburg impedance (W_1) and constant phase element Q_2 which is in parallel with resistor R_2 of the sample. R_1 represents the grain boundary resistance; R_2 represents grain resistance; Q_1 symbolize the deviance of capacitance from ideal actions. Using the equation given below the real capacitance can be calculated.

$$C = Q^{1/a} R^{(\frac{1}{a}-1)} \quad (5)$$

In the above equation, the value of exponent 'a' is between 0 and 1 which signifies the existence of non-Debye type relaxation in the sample. The fitting parameters values of R, Q and W are listed in Table 3. Compared to undoped zirconia, all Ce^{3+} doped zirconia samples showed more grain conductivity. Initially at x=0.01 and at x=0.02 (Fig. 9b and c) the sample showed decreasing conductivity, at x=0.03 (Fig. 9d) showed sudden increase, at x=0.04 (Fig. 9e) it showed a decrease and at x=0.05 (Fig. 9f) it showed a maximum conductivity. This peculiarity can be clarified in the following way. When Ce^{3+} ions are doped into zirconia, for charge neutrality, one oxygen vacancy is formed for every one Ce^{3+} ion, which may be symbolized by the Kröger–Vink notation.

$$Ce_2O_3 \rightarrow 2Ce'_{Zr} + 3O_O^x + V_0^{\cdot\cdot} \quad (6)$$

$$[Ce'_{Zr} = 2V_0^{\cdot\cdot}] \quad (7)$$

where Ce'_{Zr} represents Zr^{4+} site occupied by Ce^{3+} ion and $V_0^{\cdot\cdot}$ is the oxygen vacancy. In a recent study [18] it has been reported that oxygen vacancies ($V_0^{\cdot\cdot}$) increase with doping concentration. Therefore, with the more of Ce^{3+} ion concentration the conductivity increases and reaches a maximum value at x=0.05. It was observed that at x=0.04 the conductivity decreases which is due to a greater number of interactions between Ce^{3+} ions and oxygen vacancies and formation of local defect structures which lower the mobile oxygen vacancies [19]. The formation of dimers($Ce'_{Zr} - V_0^{\cdot\cdot}$) are responsible for the associated enthalpy at lower concentration of Ce^{3+} ions. In the same way the probability of formation of trimers ($Ce'_{Zr} - V_0^{\cdot\cdot} - Ce'_{Zr}$) becomes high for higher concentrations of Ce^{3+} ions (at x=0.04) since the concentration of Ce^{3+} ions grow double the oxygen vacancies. Therefore, the decrease in conductivity is mainly due to increase in establishment of trimers and local defect structures with more and more of Ce^{3+} ion concentration.

Table 4 The fitting parameters values of R, Q and W for undoped and Ce^{3+} doped ZrO_2 samples

R_s + $Q_1/(R_1+W_1)$+ Q_2/R_2	Rs (ohm)	Q_1 (F.s^(a - 1))	a_1	R_2 (Ohm)	Q2 (F.s^(a - 1))	a_2	R_2 (Ohm)	W_1 (Ohm.s-^1/2)
Un doped ZrO_2	123	8.418e-9	0.7234	113136	0.1384e-9	0.8168	109357	5.792e6
ZrO_2:Ce^{3+} (1 mol %)	95	4.05e-9	0.7734	72348	0.133e-9	0.8122	127743	8.749e6
ZrO_2:Ce^{3+} (2 mol %)	90	0.226 7e-9	0.785	790979	4.292e-9	0.7672	565550	7.437e6
ZrO_2:Ce^{3+} (3 mol %)	92	14.45e-12	1	9865	0.2512e-6	0.5146	10.65e6	0.256 7e6
ZrO_2:Ce^{3+} (4 mol %)	94	4.701e-6	0.2492	1799	0.2485e-9	0.77	49700	86814
ZrO_2:Ce^{3+} (5 mol %)	92	2.354e-6	0.3428	1.162e6	0.2895e-9	0.7831	17871	1.731e6

The dielectric constant (ε') and the ac conductivity (σ_{ac}) of the samples were calculated using the following formulae.

$$\varepsilon' = (C\ d)/(\varepsilon_o A) \quad (8)$$

$$\sigma ac = G \times \frac{d}{A} \quad (9)$$

where C is the capacitance, d is thickness, G is conductance, ε_o is absolute permittivity and A is area of the pellets. The dielectric constant (ε') response as a function of frequency (log f) of undoped and doped Zirconia is as shown in Fig. 10.

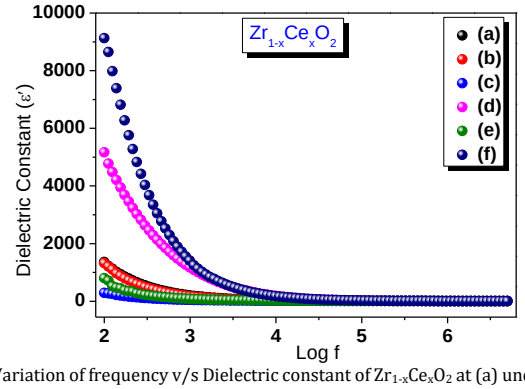

Fig. 10 Variation of frequency v/s Dielectric constant of $Zr_{1-x}Ce_xO_2$ at (a) undoped (b) x=0.01 (c) x=0.02 (d) x=0.03 (e) x=0.04 and (f) x= 0.05 molar concentrations

All the samples were showing high dielectric constant at low frequencies because at the interface, electrolyte and electrode contribute to oxygen ions polarization. As the frequency increases the dielectric

https://doi.org/10.30799/jnst.220.19050201

Cite this Article as: H.C. Madhusudhana, S.N. Shobhadevi, B.M. Nagabhushana, R. Hari Krishna, M.V. Murugendrappa, H. Nagabhushana, Structural and dielectric investigations of cerium stabilized zirconia ($Zr_{1-x}Ce_xO_2$(x=0-0.05)) nanocrystals blended by wet chemical method, J. Nanosci. Tech. 5(2) (2019) 649–654.

constant decreases rapidly and becomes saturated at high frequency region for all the samples. High dielectric constant (ε' = 50) was observed for the sample at x=0.05 (5 MHz) and low dielectric constant (ε' = 18) was observed for undoped ZrO_2 (5 MHz). The value of high dielectric constant at lower frequencies is due to the contributions from the space charge, dipolar, ionic and electronic polarizations [20]. Space charge polarization is generally responsive at lower frequencies and the frequency dependent dielectric constant may be explained on the basis of space charge polarization phenomenon [21].

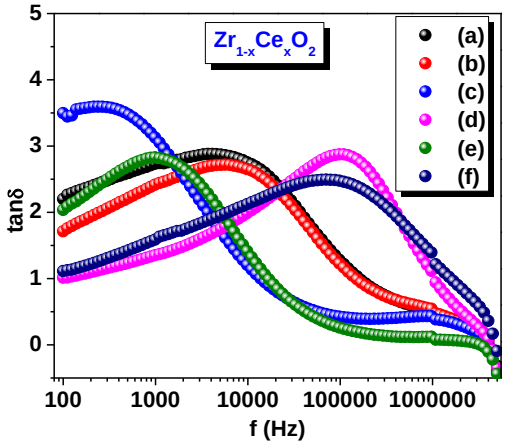

Fig. 11 Variation of frequency v/s loss tangent of $Zr_{1-x}Ce_xO_2$ at (a) undoped (b) x=0.01 (c) x=0.02 (d) x=0.03 (e) x=0.04 and (f) x= 0.05 molar concentrations

Fig. 11 shows the variation of dielectric loss of $Zr_{1-x}Ce_xO_2$ (x=0-0.05) with respect to frequency. It indicates the presence of a lone relaxation peak, which may be due to the dipole moment of the defect pair ($Ce'_{Zr} - V_O^{\cdot\cdot}$). At higher frequency, because the dipoles cannot re-orient themselves to the applied frequency, the tangent loss (tanδ) value becomes independent. The relaxation peak shifts towards high frequency region from undoped Zirconia to all other doped Zirconia samples. The intensity of the peak is increasing due to increased oxygen vacancies and also due to the defect pair which might be unrestricted from defect trimers ($Ce'_{Zr} - V_O^{\cdot\cdot} - Ce'_{Zr}$)[22]. This results in higher grain conductivity due to oxygen vacancies which execute local motions around Ce^{3+}dopant giving rise to long range migrations. This type of shifting of relaxation peaks is explained by H. Yamamura et al. in an earlier report, according to which the relaxation peaks at higher frequency side corresponds to defect pair such as ($Ce'_{Zr} - V_O^{\cdot\cdot}$) and relaxation peaks at lower frequency side are due to neutral trimers such as ($Ce'_{Zr} - V_O^{\cdot\cdot} - Ce'_{Zr}$) [23]. This shows that oxygen vacancy and dopants have columbic interaction, hence, depending on Ce^{3+} ion concentration, the relaxation peak shifts to higher frequency region due to the variation in defect pairs.

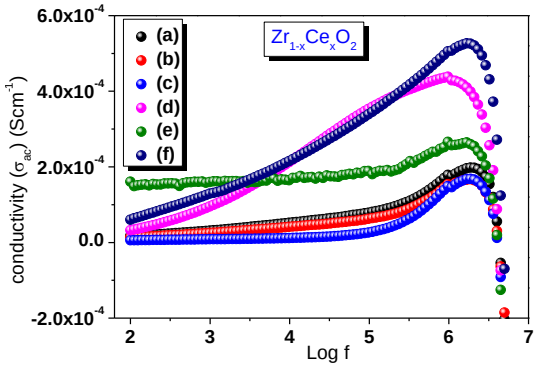

Fig. 12 variation of frequency v/s conductivity of $Zr_{1-x}Ce_xO_2$ at (a) undoped (b) x=0.01 (c) x=0.02 (d) x=0.03 (e) x=0.04 and (f) x= 0.05 molar concentrations

Fig. 12 shows the variation of ac conductivity (σ_{ac}) with frequency. As seen from the figure, the ac conductivity has a small value at lower frequencies and increased at higher frequencies. It has a maximum value at 10 MHz for Ce doped ZrO_2 having low dispersion which is reflecting in dielectric constant. Incorporation of Ce^{3+} ions to the host lattice Zr^{4+} creates more defects in the crystals which also contribute to the increase in conductivity. The ac conductivity increases at higher frequency and after a certain limit, it responds according to Jonscher's power law [24] which is given by,

$$\sigma'(\omega) = \sigma_{dc} + A\,\omega^{n} \qquad (10)$$

where n is frequency exponent and A is the pre-exponential factor. With the help of Jump relaxation model, conductivity of all the samples can be explained based on previous reports [25]. The dielectric constant ε'(ω) and ac conductivity σ'(ω) variation with respect to doping concentration is shown in the Fig. 13.

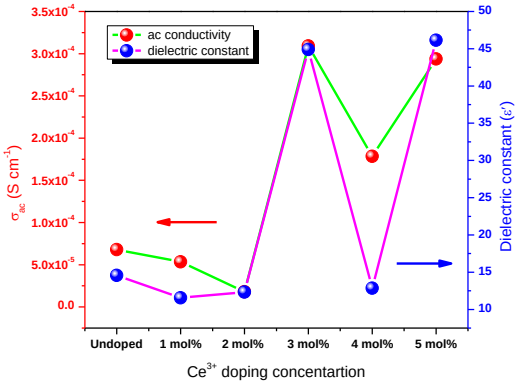

Fig. 13 Variation of ac conductivity (σ_{ac}) and dielectric constant (ε') v/s doping concentrations

Since the dielectric constant and ac conductivity are closely related, they respond in a similar way with respect to doping concentration. It was observed that both conductivity and dielectric constant have a maximum value for a particular composition. This may be because of oxygen vacancy and lattice ion columbic interaction and is represented by the equation,

$$F = \frac{-2\,e^2}{4\pi\varepsilon r^2} \qquad (11)$$

Here dielectric constant is represented by 'ε' and inter ionic distance is 'r'. The expression specifies that if the dielectric constant is small, the columbic interaction between dopant ions and oxygen vacancies becomes high, which results in enhanced activation energy and reduced conductivity. At x=0.05 (Fig. 10) has less columbic interaction and more conduction compared to all other samples and it has the highest value of ε'(ω) at frequency 5 MHz. For x=0.0, σ'(ω) is lower than Ce^{3+}doped Zirconia due to the lower value of ε'(ω).

4. Conclusion

In summary, $Zr_{1-x}Ce_xO_2$ (x=0-0.05) nanocrystals were prepared by low cost wet chemical method. XRD data matches with JCPDS file No. 27-0997 confirming the crystal structure of the sample as cubic phase. The SEM images showed the samples are irregular in shape and agglomerated. The impedance spectra were analyzed using suitable RQ circuit and found that both the grain and grain boundary contribution were present in the materials. Impedance analysis also confirmed the non-Debye type relaxation in the materials. The variation of conductivity was correlated with oxygen vacancies and defect associates. The shift of the relaxation peak of tanδ with doping concentration has been explained in the light of formation of dimers or trimers and evolution of oxygen vacancies. The relaxation peak in modulus spectra was attributed to the charge re-orientation relaxation of defect pairs. The conductivity values, dielectric and modulus properties of pure zirconia were compared to that of Ce^{3+} doped zirconia. The conductivity values and dielectric properties showed x = 0.05 as the optimum doping concentration in our present system.

Acknowledgements

H.C. Madhusudhana is grateful to the Principal, Dayananda Sagar Academy of Technology and Management for their continuous support and encouragement. The author is thankful to the Dr. P. Aruna, Asst. Professor, Dept. of Physics, DSCE, Bangalore, for her valuable suggestions in all characterization analysis.

References

[1] S.Z. Ajabshir, M.S. Niasari, Facile route to synthesize zirconium dioxide (ZrO_2) nanostructures: structural, optical and photocatalytic studies, J. Mol. Liq. 216 (2016) 545-551.
[2] M. Gawande, A. Rathi, P. Branco, Nano MgO-ZrO_2 mixed metal oxide, characterization by SIMS and application in the reduction of carbony1 compounds and in multicomponent reaction, RSC Adv. 3 (2013) 3611-3617.
[3] G. Guo, Y. Chen, A nearly pure monoclinic nanocrystalline zirconia, J. Solid State Chem. 178 (5) (2005) 1675-1682.

https://doi.org/10.30799/jnst.220.19050201

Cite this Article as: H.C. Madhusudhana, S.N. Shobhadevi, B.M. Nagabhushana, R. Hari Krishna, M.V. Murugendrappa, H. Nagabhushana, Structural and dielectric investigations of cerium stabilized zirconia ($Zr_{1-x}Ce_xO_2$(x=0-0.05)) nanocrystals blended by wet chemical method, J. Nanosci. Tech. 5(2) (2019) 649–654.

[4] G. Pratap, D. Kajale, V. Patil, G. Patil, G. Jain, Synthesis and nanostructure ZrO_2 for gas sensing application, J. Smart Sens. Intell. Syst. 5 (3) (2012) 673-683.
[5] S. Manjunatha, M.S. Dharmaprakash, Synthesis and characterization of Cerium doped ZrO_2 blue-green emitting nanophosphors, Mater. Lett. 164 (2016)476–479.
[6] Geoffrey A. Tompsett, Nigel M. Sammes, Osamu Yamamoto, Ceria–yttria-stabilized zirconia composite ceramic systems for applications as low-temperature electrolytes, Jour. Am. Ceram. Soc. 80 (1997) 3181-3186.
[7] A.L. Patterson, The Scherrer formula for X-ray particle size determination, Phys. Rev. 56 (1939) 978-982.
[8] G.K. Williamson, W.H. Hall, X-ray line broadening from filed aluminium and wolfram, Acta. Metall. 1 (1953) 22–31.
[9] D. Prakashbabu, R. Harikrishna, B.M. Nagabhushana, H. Nagabhushana, C. Shivakumara, et al., Low temperature synthesis of pure cubic ZrO_2 nanopowder: Structuraland luminescence studies, Spectrochim. Acta: A 122 (2014) 216–222.
[10] I.A. Siddiquey, T. Furusawa, M. Sato, N.M. Bahadur, Md. Nizam Uddin, Noboru Suzuki, A rapid method for the preparation of silica-coated ZrO_2 nanoparticles by microwave irradiation, Ceram. Int. 37 (2011) 1755–1760.
[11] Jiahe liang, Zhaoxiang Deng, Photoluminescence of tetragonal ZrO_2 nanoparticles synthesized by microwave irradiation, Inorg. Chem. 41 (2002) 3602–3604.
[12] Jun Zhang, Junhua Xi, Zhenguo Ji, Mo + N Codoped TiO_2 sheets with dominant {001} facets for enhancing visible-light photocatalytic activity, J. Mater. Chem. 22 (2012) 17700-17708.
[13] H.T. Zhang, G. Wu, X.H. Chen, Thermal stability and photoluminescence of $Zr_{1-x}Ce_xO_2$ ($0 \leq x \leq 1$) nanoparticles synthesized in a non-aqueous process, Mater. Chem. Phys. 101 (2007) 415–422.
[14] S. GirishKumar, K.S.R. Koteswara Rao, Zinc oxide based photocatalysis: tailoring surface-bulk structure and related interfacial charge carrier dynamics for better environmental applications, RSC Adv. 5 (2015) 3306–3351.
[15] K.C. Verma, M. Ram, J. Singh, R.K. Kotnala, Impedance spectroscopy and dielectric properties of Ce and La substituted $Pb_{0.7}Sr_{0.3}$ $(Fe_{0.012}Ti_{0.988})$ O_3 nanoparticles, J. Alloys Compd. 509 (2011) 4967-4971.
[16] K. Funke, Ion transport in fast ion conductors - spectra and models, Solid State Ionics 94 (1997) 27-33.
[17] S. Sayan, N.V. Nguyen, J. Ehrstein, T. Emge, E. Garfunkel, et al., Structural, electronic, and dielectric properties of ultrathin zirconia films on silicon, Appl. Phys. Lett. 86 (2005) 152902-152903.
[18] S.K. Anirban, T. Paul, A. Dutta, Vacancy mediated ionic conduction in disubstituted nanoceria: a structure–property correlation study, RSC Adv. 5 (2015) 50186-50195.
[19] S. Ramesh, K.C. James Raju, Preparation and characterization of Ce_{1-x} $(Gd_{0.5}Pr_{0.5})$ XO_2 electrolyte for IT-SOFCs, Int. J. Hydro. Ener. 37 (2012) 10311-10317.
[20] S. Sagadevan, C. Arunseshan, Investigations on synthesis, structural, morphological and dielectric properties of manganese oxides nanoparticles, Appl. Nanosci. 4 (2014) 179–184.
[21] S. Sagadevan, Synthesis, structural and dielectric properties of zinc sulfide nanoparticles, Int. J. Phys. Sci. 8 (2013) 1121-1127.
[22] A.K. Baral, H.P. Dasari, B.K. Kim, J.H. Lee, Effect of sintering aid (CoO) on transport properties of nanocrystalline Gd doped ceria (GDC) materials prepared by co-precipitation method, J. Alloys. Compd. 575 (2013) 455-460.
[23] H. Yamamura, S. Takeda, K. Kakinuma, Dielectric properties of proton conductor $BaCe_{0.9}Y_{0.1}$ $O_{3-\delta}$, Solid State Ionics 178 (2007) 889-893.
[24] A.K. Jonscher, The 'universal' dielectric response, Nature 267 (1977) 673-679.
[25] K. Funke, Ion transport in fast ion conductors-spectra and models, Solid State Ionics 94 (1997) 27-33.

https://doi.org/10.30799/jnst.220.19050201

Cite this Article as: H.C. Madhusudhana, S.N. Shobhadevi, B.M. Nagabhushana, R. Hari Krishna, M.V. Murugendrappa, H. Nagabhushana, Structural and dielectric investigations of cerium stabilized zirconia ($Zr_{1-x}Ce_xO_2$(x=0-0.05)) nanocrystals blended by wet chemical method, J. Nanosci. Tech. 5(2) (2019) 649–654.